

Multiplexed Biosensing of Proteins and Virions with Disposable Plasmonic Assays

Stephanie Wallace,¹ Martin Kartau*,¹ Tarun Kakkar,¹ Chris Davis,³ Agnieszka Szemiel,³ Emmanuel Mailart,⁴ Kevin Gautier,¹ Adrian J. Lapthorn,¹ Nikolaj Gadegaard,² Malcolm Kadodwala,¹ Edward Hutchinson,³ Affar S. Karimullah*,¹

1. School of Chemistry, University of Glasgow, Joseph Black Building, University Avenue, G12 8QQ, Glasgow, UK
2. James Watt School of Engineering, University of Glasgow, Rankine Building, Oakfield Avenue, G12 8LT, Glasgow, UK
3. MRC-University of Glasgow Centre for Virus Research, 464 Bearsden Road, G61 1QH, Glasgow, UK
4. HORIBA France SAS, 14, Boulevard Thomas Gobert - Passage Jobin Yvon, CS 45002 – 91120, Palaiseau, France

Abstract

Our growing ability to tailor healthcare to the needs of individuals has the potential to transform clinical treatment. However, the measurement of multiple biomarkers to inform clinical decisions requires rapid, effective, and affordable diagnostics. Chronic diseases, and rapidly evolving pathogens in a larger population have also escalated the need for improved diagnostic capabilities. Current chemical diagnostics are often performed in centralised facilities and are still dependent on multiple steps, molecular labelling, and detailed analysis causing the result turnaround time to be over hours and days. Rapid diagnostic kits based on lateral flow devices can return results quickly but are only capable of detecting a handful of pathogens or markers. Herein we present the use of disposable plasmonics as a platform for low-cost label-free optical biosensing with multiplexing capabilities, eliminating the need for flow systems often required in current optical biosensors. We demonstrate the biosensing capabilities of a system that uses chiroptical measurements as well as plasmonic enhanced fluorescence from metafilms with shuriken shaped nanoindentations. We also perform detection of SARS-CoV-2 in complex solutions as an early developmental milestone towards high-throughput, single-step, diagnostic kits for differential diagnosis of multiple respiratory viruses and any other emerging diagnostic needs. Diagnostics based on this platform which we term 'Disposable Plasmonics Assays', would be suitable for low-cost screening of multiple pathogens or biomarkers in a near point of care setting.

Keywords

Biosensing; Disposable Plasmonics; Virus Diagnostics; Multiplexing.

Introduction

The use of biomarkers for precision medicine allows great advancements to aid in the improvement of human health as well as the reduction in health-care costs.^{1,2} Yet often, time, costs and capability of current technology limits the applicability of precision medicine concepts. The COVID-19 pandemic has demonstrated a need to monitor our health more regularly.³ While daily testing is not an immediate necessity, a routine approach may become the norm to maintain social healthcare standards. Polymerase chain reaction (PCR) diagnostic approaches are currently the gold standard of infectious disease diagnostics but their cost and turnaround time make them impractical for use in large scale routine testing. PCR has a relatively lengthy response time and, when in high demand, has the potential risk for global shortage of oligonucleotide reagents as seen in the SAR-CoV-2 pandemic.⁴ It has been argued that sensitivity should be secondary compared to test frequency for large scale population testing.⁵ Modelling of the current SARS-CoV-2 pandemic indicates that such a strategy is theoretically capable of reducing the R number of an epidemic.^{5,6} Furthermore, because PCR detects nucleic acids it cannot directly provide information about the proteome and other non-DNA/RNA based disease markers. Sensitive diagnostics for proteins and other biomarkers is still largely dependent on laborious techniques based on chemical assays or mass spectrometry. Such methods typically require a significant investment of reagents, samples, and time, making them costlier and less efficient.⁷

Rapid and economical detection of some pathogen components and biomarkers has been achieved using lower sensitivity tests such as lateral flow devices (LFDs) and traditional immunoassays (e.g. ELISA) which are now well established for non-PCR based diagnostics. Yet, when applied to more than a single disease, these methodologies are either not high-throughput or require multiple reagents and lack ease of use. These technological limitations are a bottle neck in our progress towards being able to test rapidly for multiple pathogens with high-throughput and low costs. LFDs have made a significant step towards readily available mobile testing and is arguably the most cost effective and simplest testing technique.^{3,8} LFDs require multiple antibodies plus label/colour producing reagents which often suffers from reduced sensitivity and reliability.^{3,7,9} Furthermore, the diffusion based paper flow methodology limits the ability to add additional tests in a small area due to interference of flow paths and/or interference between sequential detection sites if positioned within a common flow path.¹⁰ Hence, multiple testing with LFDs either have complicated manufacturing methods or lead to large dimensions increasing cost and reducing mobility and hence, limiting them to detecting a single biomarker that also generate a large quantity of waste in packaging.¹⁰

Optical based biosensing was long heralded as the best route to label-free sensitive PoC multiplexed diagnostics.¹¹ Using the overlap between analytical chemistry and optical sensing, plasmonics sensors can detect interactions between a monolayer of surface immobilised binders and their target biomarkers. Due to their label-free sensing capability, the only reagents required are a buffer and the antibody/binder. A variety of plasmonic based techniques have been implemented such as Surface Plasmon Resonance (SPR), Surface Enhanced Raman Spectroscopy (SERS), Localised Surface Plasmon Resonance (LSPR), and plasmonics based colorimetric assays.⁷ SPR based biosensors have been the most successful with surface functionalisation techniques to enhance specificity between biomarkers and surface attached ligands and achieved diagnostics of diseases such as AIDS and Hepatitis.^{12,13} They only require binder immobilisation and buffers as reagents and are not dependant on adding any nanoparticles or additional steps such as mixing or rinsing. However, SPR biosensors have drawbacks involving limited portability, bulky liquid handling systems, and high sample volume requirements, which limits their practicality in PoC settings.¹⁴ LSPR devices were

supposed to mitigate these issues but have often suffered difficulties such as reduced sensitivity to refractive indices. Complex nanostructure design could potentially allow for high quality factors and improved sensing performances but are restricted due to high manufacturing costs of consumables and reproducibility problems. A large amount of LSPR sensors are still based on nanoparticles in solutions or colloidal Au based films but have started seeing success with companies such as LamdaGen and Nicoya for the biosensor market.^{14–18} In terms of PoC diagnostics commercially, to the best of our knowledge, only Genalyte has been able to successfully use a photonics sensor to provide label-free multiplexed diagnostics, albeit still using a relatively complex and expensive consumable based on split-ring resonators on Si substrates.¹⁹ Plasmonic based PoC still remains elusive due to the complexities and costs.

Herein, we report on the use of injection moulded nanopatterned polycarbonate templates, with complex nanostructure geometries, for use in multiplexed biosensing of proteins and virions as a proof of concept for the development of a multiplexed low-cost diagnostics platform. These low-cost templated plasmonic substrates (TPS) are capable of large-scale multiplexing with high surface sensitivity allowing the development of multi-pathogen diagnostic assays that we call ‘Disposable Plasmonic Assays’ (DPAs). We performed label-free biosensing without any flow setup or microfluidics demonstrating the potential of DPAs to be used as a simplified platform for PoC diagnostics. The disposable plasmonics concept has previously been used for chiral plasmonic sensing, a technique that uses chiral nanostructures with biostructural sensitivity to measure protein binding interactions. In this work, we use the chiral nanostructures for their sharp optical rotation dispersion (ORD) response with their high figure of merit (FOM) that enable better automated peak detection and performance for label-free measurement. The chiral nanostructures used have high refractive index sensitivity (~ 400 nm/RIU) and surface sensitivities as their fields decay significantly by ~ 25 nm above the sensor surface. Using a hyperspectral polarimetry imaging instrument, we were able to measure multiple nanostructure arrays in a single experiment and mitigated the need for microfluidics by simply pipetting materials onto the sample surface. Through immobilisation of different protein binders on the arrays, this system is capable of multiplexed label-free assays that are free of any flow systems and could therefore enable single step testing. The measurement performance of the sensor platform was evaluated first, followed by label-free detection of protein binding events. The potential multiplexing capabilities were also demonstrated by the specific detection of antibodies for the SARS-CoV-2 spike glycoprotein S1 (anti-S1) and streptavidin (anti-streptavidin) in a single experiment with sequential addition of the targets. Lastly the detection of SARS-CoV-2 virions was demonstrated using functionalised antibody fragments.

Results and Discussion

Optical Characterisation

The TPS were generated by Au coating of an injection moulded plastic template. The Au film takes on the shape of the nanostructured indentations on the plastic surface producing a metafilm. The process has been used previously and described in prior literature.²⁰ Specifically, we use chiral shuriken shaped indentations as the plasmonic resonator units, Figure 1 (A-B), used in previous studies.^{21–24} They display a bisignate ORD and a ‘W’ shaped reflectivity arising from plasmonic induced reflectance.²⁴ The TPS used here are specifically designed to work with our imaging polarimetry system that recognises 9 locations labelled A to I, Figure 1(D), for multiplexing purposes. Each location has 2 nanostructured arrays, one with left-handed (LH) nanostructures and one with right-handed (RH) nanostructures. We can use LH and RH resonance shifts either to evaluate

differences for chiral plasmonic sensing or use individual resonance shifts of all 18 nanostructured arrays to gather values for our biosensing measurements. The entire measurement region is approximately a 3x3 mm square and each nanostructured array has an area of 0.09 mm² area. Solutions are added using a pipette through ports in a custom designed fluidic chamber well, and no flow systems are incorporated in the setup (Supplementary Figure 1). The imaging instrument is capable of measuring ORD and reflectivity over the visible spectrum using hyperspectral imaging and polarisation dependent filters in ~ 5 minutes. A MATLAB script automatically evaluates the ORD peaks from the measured spectra and provides peak positions and resonance shift values, (Supplementary Figure 1).

The TPS display bisignate ORD with 2 peaks that we will label Peak 1 and Peak 2, Figure 1 (E). The ORD can be used as both a means of looking at resonance shifts as well as providing biostructural sensitivity as achieved in previous studies.^{20,21} However, biostructural sensitivity requires the surface immobilised biomolecules to be aligned and achieve near homogenous orientation over the surface. This leads to an anisotropic dielectric layer surrounding the chiral nanostructures instead of one that is isotropic and leads to a measurable asymmetry.^{22,23,25} Such constraints on the immobilisation of the biomolecules can be difficult in most functionalisation strategies and this restricts the practicality of generating assays with multiple binders for multiple targets. It is also important to note that different pathogens have different physical properties. While some viruses (for example adenoviruses or picornaviruses) are transmitted within a rigid icosahedral 'capsid' assembly of proteins, others (for example influenza viruses and SARS-CoV-2) are enclosed in an envelope of lipid membrane with viral proteins on its surface. These 'enveloped virions' are typically variable in size and shape and are flexible enough to be physically deformed, leading to a lack of consistent anisotropy in the overall structure at the metal dielectric boundary.²⁶ Achieving an immobilised layer of virions that are all well aligned to provide an anisotropic dielectric layer is not universally applicable to all virions and proteins. Measurement of asymmetry would seem to be an impractical approach for rapid, robust diagnostic applications. However, chiral nanostructures, beyond their biostructure sensing capabilities, show improved figure of merit (FOM) owing to the increased complexity in resonance mechanism and show improved refractive index sensitivities. Such properties improve sensing of traditional refractive index changes.²⁷ Furthermore, the sharper ORD peaks, such as those shown by the shurikens, improve automation and collection of data from the experiment and hence our disposable plasmonic assays continue to use chiral nanostructures for biosensing based on just refractive index variations. Therefore, to measure changes in the resonance wavelength ($\Delta\lambda$) positions to detect binding events we use the ORD measurements from the shurikens. There are two inflection points in the ORD and we label these Peak 1 and Peak 2, as specified in Figure 1.

We characterised the sensing performance with sucrose solutions and the results (Supplementary Figure 1) showed a sensitivity value of ~430 nm/RIU which is between the general sensitivities of SPR (>1000 nm/RIU) and LSPR sensors (~100 nm/RIU).^{28,29} Simulations of the nanostructures (Supplementary Figure 2) also show that the electric field intensities reduce to <15% of the maximum at ~25 nm from the surface, indicating that the structures have lower decay lengths than SPR (>100nm) and similar to LSPR (~5-10nm) sensors indicating high surface sensitivities similar to LSPR sensors.¹⁵ The electromagnetic confinement shown by LSPR and our metafilm make them less susceptible to bulk changes due to effects like temperature changes or additional proteins expected in serum like samples. It also potentially provides increased sensitivity to small molecules at low concentrations.^{14,30} Hence, the shuriken metafilms combine sensing benefits of traditional LSPR and SPR biosensors.

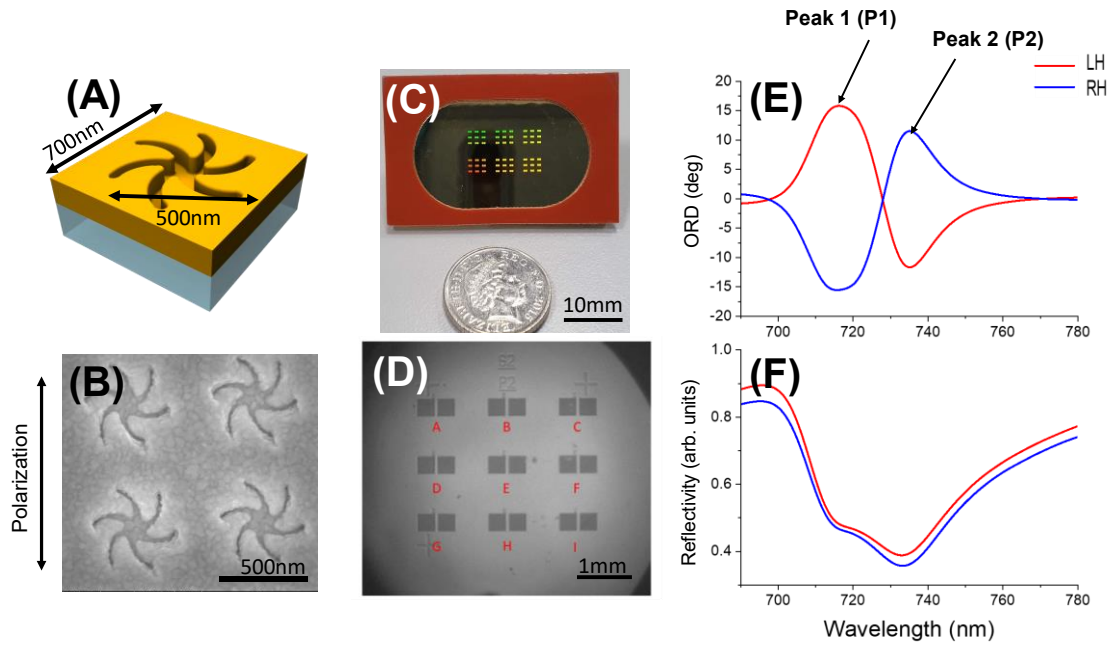


Figure 1: (A) Top of the TPS film with shuriken indentations, as shown in (B) scanning electron microscopy images. (C) Sample with multiple experimentation locations compared to a 5p coin. (D) Arrays in a single experiment as viewed by the imaging instrument for multiplexing. (E) ORD (Peak 1 and Peak 2) and (F) reflectivity spectra produced by biosensor.

To estimate the performance of the instrument and sensing substrate for a multiplexing application, we need to evaluate the noise performance and establish error limitations that will impact sensitivity and performance limits of the platform. Multiple measurements of water, followed by 2M MgSO_4 , were performed hourly and used to estimate the measurement error and potential drifts when no changes are made in the fluidic chamber. Figure 2 (A and B) and Table 1, show that the largest maximum-minimum (max-min) range is of 0.3 nm or less for both water and salt. Hence, we estimate measurement error to ± 0.15 nm for $\Delta\lambda$ of both peaks. The results also show that the errors are larger when the media is changed and resonance shifts occur, roughly giving an error in $\Delta\lambda$ of ± 0.3 nm, Figure 2(C). These may occur due to variations in incident light wave fronts, temperature and concentration gradients, or changes on the metal-liquid interface (electrical double layer) over the 3mm x 3mm measurement area that have been shown previously to affect plasmonic sensing.^{31,32} Another useful parameter to consider is the value S that represents spacing in the wavelength values between the two peaks. ΔS is the change in the spacing in comparison to the initial measurement and this has previously been used as an additional parameter to measure protein interactions at the surface.^{22,25} The large ~ 20 nm resonance shift due to MgSO_4 is accompanied by ΔS of 0.2-0.3 nm indicating a slight difference between Peak 1 and Peak 2 in terms of the sensitivity to refractive index changes. However, for proteins and buffer solutions, we expect resonance shifts to be an order smaller as the proteins form only a monolayer and the buffer solutions are far lower in salt concentration than the solutions used here. The differences in sensitivity, and hence ΔS , seen in the salt solutions would be near negligible when resonance shifts are in the order of ~ 2 -5nm.

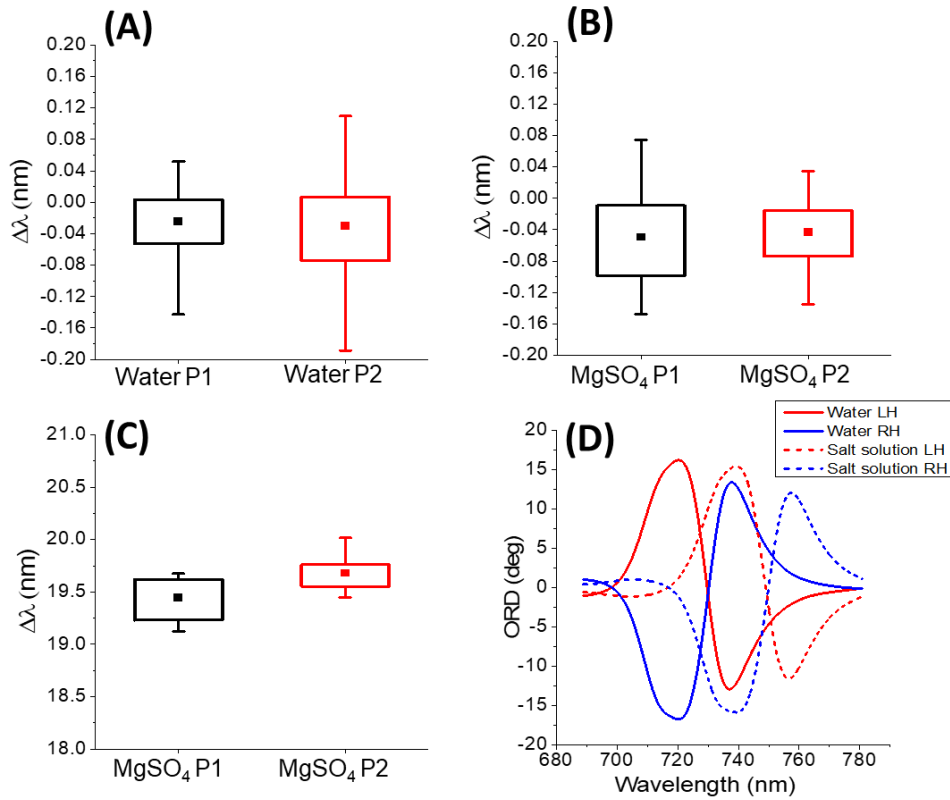


Figure 2: (A) Resonance shifts ($\Delta\lambda$) with repeat water measurements and (B) repeat MgSO_4 measurements, over 3-hour periods. (C) $\Delta\lambda$ obtained for MgSO_4 relative to water, with (D) change in ORD for both right- and left-handed structures. Boxplot whiskers show the max-min range of the data.

<u>Values in nm</u>	<u>$\Delta\lambda$ of Water over 3hrs</u>		<u>$\Delta\lambda$ of MgSO_4 relative to Water</u>		<u>$\Delta\lambda$ of MgSO_4 over 3hrs</u>	
	P1	P2	P1	P2	P1	P2
Mean $\Delta\lambda$	-0.02	-0.03	19.44	19.68	-0.05	-0.04
St.Dev. $\Delta\lambda$	0.04	0.06	0.20	0.16	0.06	0.04
Range $\Delta\lambda$	0.19	0.30	0.55	0.57	0.22	0.17
Mean ΔS	-0.01	-	0.24	-	0.01	-
St.Dev. ΔS	0.07	-	0.21	-	0.07	-

Table 1: Resonance shifts ($\Delta\lambda$) values of data shown in Figure 2. Values in nm.

Biosensing

Having calibrated the system, the sensing platform was used to measure a protein-ligand interaction namely streptavidin binding to biotin. Streptavidin binds to biotin to form one of the strongest non-covalent interactions in nature.³³ As a tetramer, streptavidin has 4 binding sites for biotin. When binding to a biotinylated SAM, it is likely to bind to only 1 or 2 biotin sites on the surface at any time due to the symmetry of the streptavidin structure and due to the surface density of biotin moieties immobilised in the SAM.³⁴ Hence, a minimum of 2 vacant sites would be expected for additional biotin to bind to the protein. Streptavidin is also expected to adopt a more compact structure upon binding to biotin.³⁵ The streptavidin-biotin interaction therefore becomes an appropriate model system to study the performance of our sensor platform.

Firstly, biotinylated PEG thiols were immobilised with spacer molecules (methyl PEG thiol) to create a (SAM) to functionalise the streptavidin onto the surface, Figure 3 (A). The spacer concentrations were optimised to completely inhibit non-specific interactions (Supplementary Figure 4). Unlike SPR instruments, there is no requirement for kinetic measurements to determine successful binding and experiments are performed by adding the sample for 30 mins followed by a single measurement. The peak values are evaluated by the software from the ORD spectrum during measurement and the change from the first reference water measurements are used to plot the mean $\Delta\lambda$ values. Figure 3(B) shows the resonance shifts for each peak at each step of the experiment. The SAM layer shows good adhesion to the surface with a mean $\Delta\lambda$ value of 1.6 nm for Peak 2 compared to buffer. The streptavidin (~55 kDa) is a medium sized protein and hence generates a mean of 3 nm $\Delta\lambda$ shift (Peak 2) compared to the SAM. Additional experiments performed for the same interaction showed good repeatability, Supplementary Figure 5(A-C). The streptavidin immobilisation step was followed by the addition of biotin with an Atto-655 conjugate as outlined in Figure 3 (A).

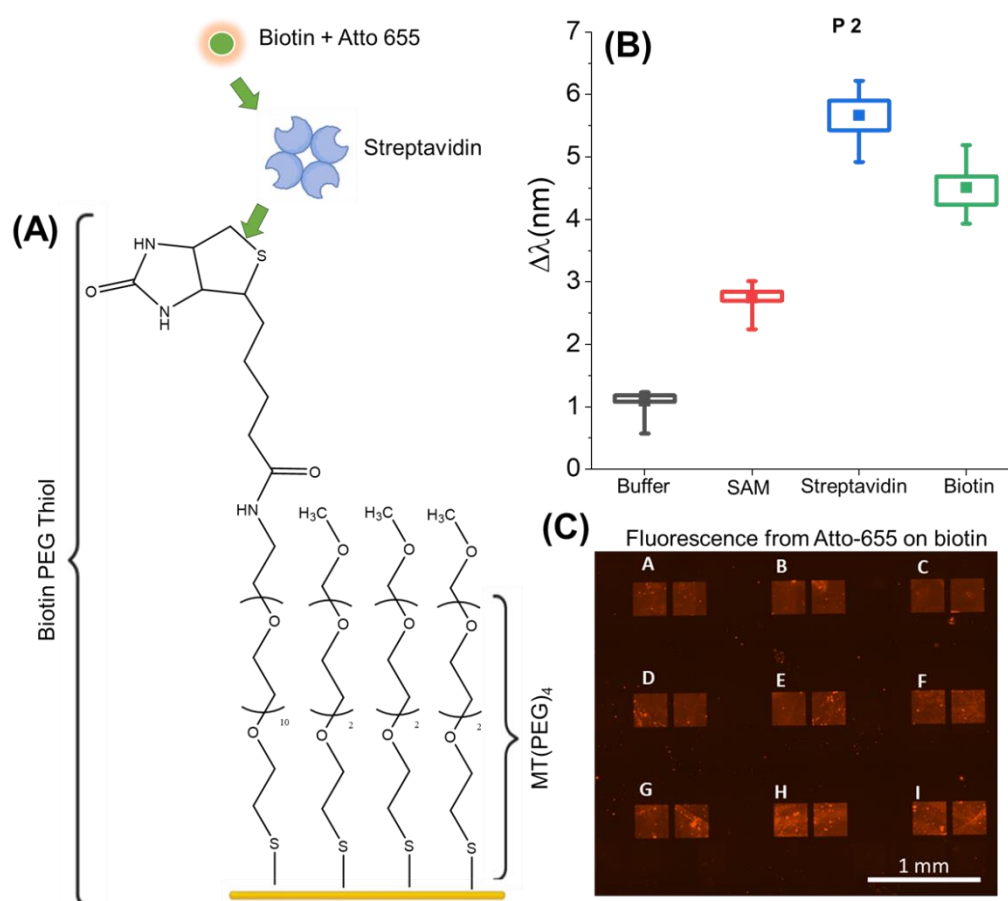


Figure 3: (A) Functionalisation and experimental scheme: Biotin PEG Thiol/MT(PEG)₄ SAM functionalised to Au surface; binding of Streptavidin to functionalised biotin; binding of Atto-655 labelled biotin to streptavidin. (B) Results for Peak 2 resonance shifts for streptavidin binding to biotin PEG thiol SAM, followed by addition of biotin (Atto-655 conjugated). Initial measurements were taken in water then buffer (PBS). Hence, all biosensing measurements are taken relative to water. Peak 2 rinsed data only shown. (C) Fluorescence from the final Atto-655 conjugated biotin observed on the nanostructures. Fluorescence over the nanostructures is more prominent due to plasmonic enhancement of the fluorescence.

Upon addition of biotin the mean resonance shifts negatively by 1.2 nm (Peak 2, 40% change in value) even though the biotin is bound to the surface immobilised tetrameric streptavidin as confirmed by the plasmonic enhanced fluorescence from the Atto-655 conjugated to the biotin, Figure 3 (C).³⁶ The negative shift could potentially arise due to dissociation of streptavidin from the surface. Given the extremely low dissociation constant of the streptavidin-biotin interaction, 10^{-15} M, this would be highly unlikely.³⁷ However, focusing on the mean ΔS values, once the relatively large streptavidin is added to the SAM, the mean ΔS increased by 0.4 nm. Yet the mean ΔS only reduced by 0.1 nm (25% change in value) when we add biotin to the surface bound streptavidin. This 25 % change in ΔS is far less than the 40 % change shown by the mean $\Delta\lambda$ and indicates that the protein has likely not been unbound from the surface in the amount indicated by $\Delta\lambda$ values, if at all. An additional experiment was performed with streptavidin conjugated with Alexa Fluor 647 (results in Supplementary Figure 5(D-E)) which showed comparable $\Delta\lambda$ values and it can be assumed that the samples have similar amounts of streptavidin on the surface given the same protocols for the SAM were used. While the dyes are different, fluorescence images show the homogenous surface coverage and similar resonance shifts values. The results indicate that the streptavidin is still bound to the surface and do not support the possibility of nearly half the streptavidin, as indicated by the 40% reduction in the resonance shift, was unbound from the surface. We hence hypothesise that the negative $\Delta\lambda$ values would be the result of structural changes (compacting) in streptavidin upon binding to additional biotin.^{35,38,39}

Multiplexing for Multi Target Diagnostics

Multiplexing in relation to biomedical diagnostics can be defined as the simultaneous measurement of multiple analytes under the same set of conditions in a single experiment and sample.¹⁶ A multiplexed target diagnostics proof-of-concept with DPAs is performed by detection of two antibody targets to their respective proteins (binders). The two binders are functionalised on a single TPS in four separate regions (two each) by dropping 500 nL volumes of the specific histidine (His)-tagged proteins onto TPS coated with a SAM made using thiolated polyethylene glycol with a nitrilotriacetic acid end group (NTA-PEG-thiol) and a methyl-PEG-thiol (MT(PEG)) spacer with a 1:4 ratio. The NTA chelating agent can bind Ni^{2+} which selectively binds the His-tagged proteins. As there are no separate compartments or fluidic systems for the binders in this DPA, the targets were added to the chamber sequentially to evaluate specific target recognition by monitoring the locations of the individual binders, as shown in Figure 4 (D).

The first of the two protein binders used was streptavidin. The second protein binder was selected to show relevance to diagnostics related for SARS-CoV-2, the virus which causes COVID. The virus particle is covered with a large number of glycosylated spike (S) proteins, that form trimeric spikes. These are promising targets for COVID antigen testing in the nasal mucus of infected individuals and its antibody tests are useful to evaluate post-infection as well. The SARS-CoV-2 spike protein is a 1273 amino acid long (180-200 kDa) class I glycoprotein which can be cleaved into two subunits, spike 1 (S1) and spike 2 (S2), which play different roles in viral binding and entry into cells. For our experimental processes, the S1 subunit was used, which consists of an N-terminal domain (NTD; amino acid sequence 14-290), and a receptor binding domain (RBD; amino acid sequence 306-527). The 193-amino acid RBD constituent of the spike protein is responsible for recognising and binding to the angiotensin-converting enzyme-2 (ACE-2) on host cells.^{40,41} Prior to its use in a multiplexed DPA, we evaluated detection of anti-S1 antibodies in more realistic samples by mixing the antibodies in an artificially reconstituted mimic of human mucus, containing 0.2% mucin, plus 0.25 mg/ml

haptoglobin and 0.50 mg/ml transferrin in phosphate buffer saline (PBS). The binders were tested against His-tagged recombinant S1-protein immobilised over the whole surface. Each measurement was taken relative to the SAM measurement after rinsing with PBS and Tween 20 solution to remove any non-specifically bound material on the surface, shown in Figure 4 (B) (Peak 1 and additional data in Supplementary Figure 7). A mean $\Delta\lambda$ value of 2.6 nm (Peak 2) was obtained for the successful immobilisation of the S1-protein onto the SAM. The artificial mucus was then applied for 15 minutes as a control to monitor any non-specific binding. Measurements with the artificial mucus itself shows non-specific binding with mean $\Delta\lambda$ of 0.2 nm (Peak 2), values similar to resonance shift error (± 0.3 nm) expected for changes in media performed previously. These are also much smaller than the expected shifts (>2 nm) for anti-S1 antibodies (anti-S1 Ab) that are >100 kDa in mass. The artificial mucus was spiked with a 1 μ M solution of anti-S1 Ab and applied to the biosensor for one hour in which positive shifts of 1.2nm (Peak 2) were observed for the change in the mean $\Delta\lambda$, portraying binding of the anti-S1 Ab to the S1 protein. From the data displayed in Figure 4 (B), there is minimal variance across the 9 structures, portrayed by the box plots (25-75% quartile shown by the box and max-min range by the whiskers) indicating a similar response from all arrays at each stage of the experiment. In particular, the anti-S1 Ab maximum and minimum data lies within a 0.3 nm range for Peak 2.

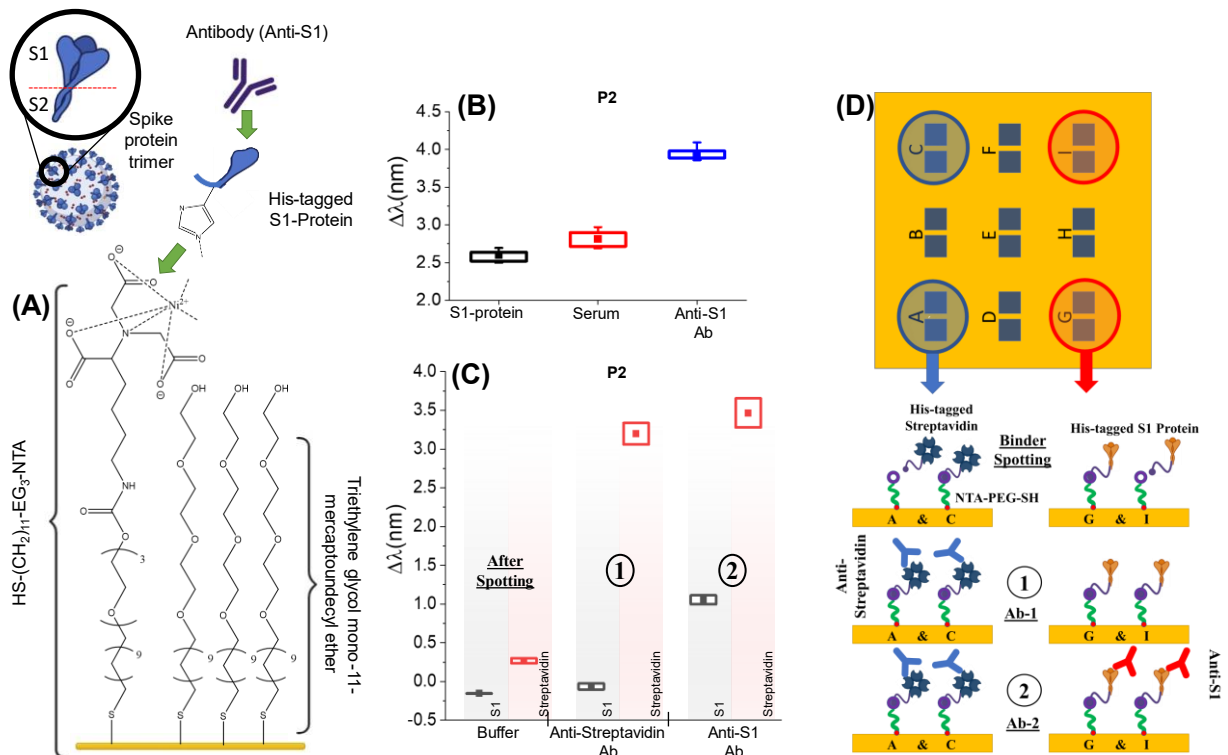


Figure 4: (A) Functionalisation and experimental scheme of functionalised NTA/EG-thiol SAM being used to bind histagged S1-protein that is then used as an antigen test to detect anti-S1 IgG antibodies. (B) Results for 1 μ M S1-protein binding to pre-functionalised NTA/EG-thiol SAM, followed by addition of artificial mucus, which was then spiked with 1 μ M Anti-S1 Ab. Mean $\Delta\lambda$ values were taken relative to water. (C) Multiplexed DPA biosensing results showing mean $\Delta\lambda$ values with sequential addition of target antibodies for histagged S1-protein (red regions) and histagged streptavidin (blue regions) spotted onto pre-functionalised NTA/EG-thiol SAM. This is followed by addition of spiked artificial mucus with Step 1) 1 μ M Anti-streptavidin Ab and then Step 2) 1 μ M Anti-S1 Antibody. Peak 2 rinsed data only. (D) Graphical description of the experiment with sequential addition of the two targets.

After successful confirmation of the immobilisation strategy and testing S1-protein interaction with anti-S1 Ab in artificial mucus, the multiplexing arrangement, or multiplexed DPA, was completed with streptavidin immobilised on locations A and I, and S1-protein immobilised on locations G and I, Figure 4 (D). All other locations were ignored.

Measurements after PBS rinsing are shown in Figure 4 (C) where all values are the average of the two locations for each target relative to the initial buffer measurements. Each target antibody (1 μM) was spiked in artificial mucus and was introduced sequentially (Step 1 for anti-streptavidin and Step 2 for anti-S1) into the chamber and left for 15 minutes, then rinsed with PBS after which the measurements were performed. Addition of the anti-streptavidin Ab, Step 1, incurred minimal non-specific binding of this antibody to the S1 protein (change in mean $\Delta\lambda$ is 0.1 nm Peak 2), whilst specific binding to streptavidin showed a change in mean $\Delta\lambda$ of 3 nm (Peak 2) was observed. Immobilisation of the Anti-S1 Ab thereafter bound only to the S1 protein giving a change in mean $\Delta\lambda$ of 1.2 nm while the streptavidin regions showed change in mean $\Delta\lambda$ of only 0.3 nm due to potential non-specific interactions. The values are similar to the previous experiment shown in Figure 4 (B). These results validate the specific detection capabilities of this multiplexing setup with the potential to detect various biomolecules within one experimental setup using binders coated onto specific regions without the need of kinetic measurements or flow systems required in SPR.

It should be noted from Figure 4 (C) that the resonance shifts exhibited for the Anti-S1 Ab are significantly smaller in comparison to those obtained for the Anti-streptavidin Ab, although both have a molecular weight of ~ 150 kDa.⁴² This is likely due to the variation in coverage on the surface, hence, providing fewer epitopes for the antibodies to bind to. It is likely to be further compounded by variations in the antibody affinities for their targets.

Detecting Inactivated SARS-CoV-2 Virions

Next, we evaluated the biosensor platform for use in viral diagnostics. Additionally, we assess whether it could detect intact virions. These biological structures are substantially larger and more complex than individual proteins, and if they could be detected directly it would remove need for lysis of samples, reducing the processing step required in detection. As an example, we targeted the SARS-CoV-2 virion for our DPA. Antibodies are the classic binders used in most immunoassay diagnostics and here we use the anti-S1 Ab as the binder. However, instead of functionalising antibodies through chemical moieties in our SAM, we use a simpler approach by immobilising Fab' antibody fragments directly onto the Au surface.²³ This reduces the need for additional functionalisation steps saving time and materials. SARS-CoV-2-binding antibodies were cleaved using immobilised pepsin. This nonspecific endopeptidase produces F(ab')_2 fragments by enzymatically digesting the Fc portion of the IgG below the hinge region. The F(ab')_2 fragments are made up of 2 Fab' fragments that contain the antigen-binding sections of the antibody joined together by disulphide bonds. Upon addition of the F(ab')_2 fragments to the Au surface, the disulphide bridges oxidise to form F(ab') fragments, in which the freed sulfhydryl groups facilitate attachment to the gold surface providing an attachment point for the antigens, using the protocol outlined in Figure 5(A). Hence, the Fab' fragment can be directly functionalised onto the TPS to develop a DPA for detection of SARS-CoV-2 viruses with the biosensor.

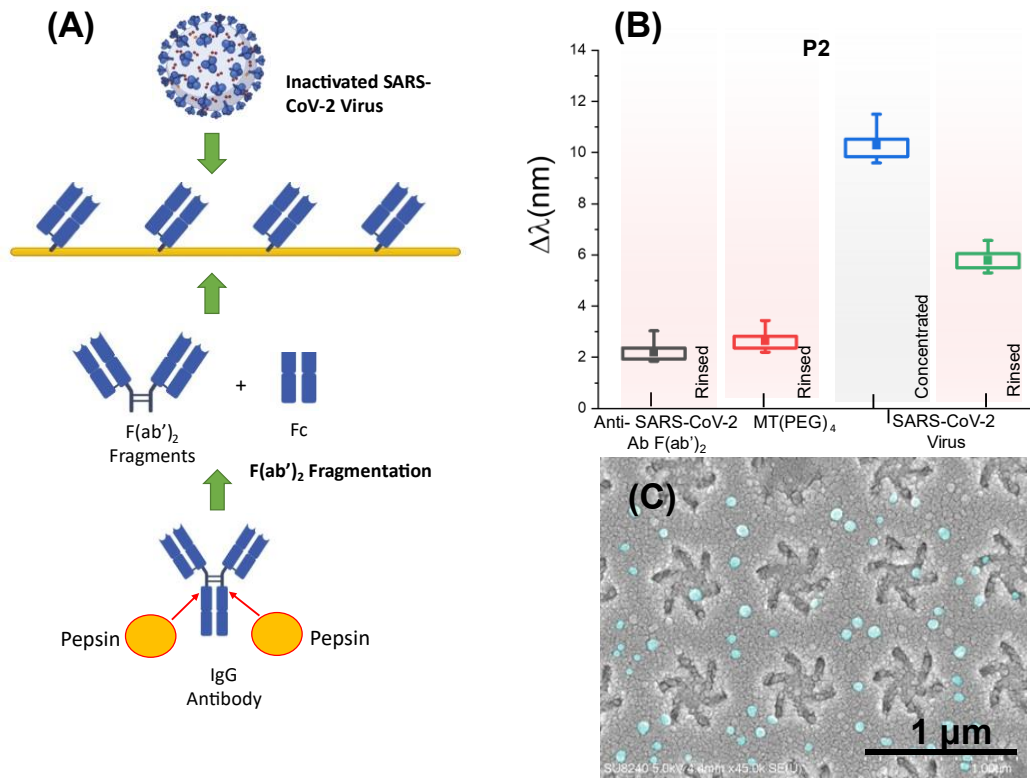


Figure 5: (A) Description of polyclonal $F(ab')_2$ fragmentation and its functionalisation which is then used for detecting inactivated SARS-CoV-2 Virus. The MT(PEG)₄ spacer is not shown. (B) Results for inactivated SARS-CoV-2 virion detection experiment. The biosensing measurements were taken relative to an initial buffer measurement. Peak 2 data shown. (C) SEM of nanostructures with virion coverage across surface. Prominent viruses are highlighted in false colour (cyan).

The $F(ab')_2$ fragment solution (Anti-SARS-CoV-2 Spike Glycoprotein S1 antibody) was added to the TPA sample for 2 hours, followed by addition of 2mM MT(PEG)₄ for 2 hours to completely passivate the sample, preventing any non-specific binding of the virus which was added thereafter for 1 hour. The chamber was rinsed using buffer (PBS) and measurements were taken. Figure 5 (B) shows the mean $\Delta\lambda$ values for Peak 2 (Peak 1 in Supplementary Figure 11). A 2.2 nm mean $\Delta\lambda$ value was obtained for the binding of Anti-SARS-CoV-2 to the DPA, with a further 0.4 nm for the MT(PEG)₄ spacer.

The clinical isolate SARS-CoV-2-CVR-GLA-8 was amplified to a titre of 7.3×10^5 plaque forming units (PFU) / ml (details in methodology). The virions were inactivated in formaldehyde for 30 min to allow safe handling, after which excess formaldehyde was quenched by diluting 1:1 with 50 mM Tris buffer resulting in final sample with $\sim 3 \times 10^5$ inactivated virions per ml. After addition of the SARS-CoV-2 virus, a measurement with the viral solution was taken (concentrated) in addition to a measurement after a buffer rinse. Addition of the diluted SARS-CoV-2 solution to the DPA yielded a 7.7 nm $\Delta\lambda$ when taking a measurement with the virus solution (concentrated) after 1 hour, which reduced by 3.8 nm upon rinsing with buffer. This reduction in resonance shift is indicative of the removal of non-specifically bound virions, implying that the final resonance shifts represent specifically bound virus material on the DPA. The SEM taken of the sample (Figure 5 (C)) shows small spherical particles (~ 50 -100 nm in diameter, false coloured in cyan) on the shuriken structures, indicative of virions, further reinforcing the resonance shifts obtained post rinsing.

Conclusions

The concept of DPAs could provide a mass manufacturable route to cheaper and reliable label-free biosensors for diagnostics. Our shuriken metafilms have shown attributes of LSPR and SPR sensors and the biosensing results here prove the validity and accuracy of multiplexed plasmonic biosensing using these substrates. Our platform based on a hyperspectral imaging instrument and the TPS consumable was used successfully to detect protein-protein interactions with high sensitivity to interactions at the surface. Using this platform, a simple DPA was created with multiple functionalised binders for an antibody target detection exemplar that successfully detected antibodies in complex artificial mucus like conditions. The direct detection of virions without lysing or any additional labelling was also successfully demonstrated paving the way for future development of a multiplexed virus detection DPA. The DPA uses antibodies directly functionalised to the surface further mitigating the number of reagents required. With increased multiplexing, DPAs can be developed for large target screening assays. Through this approach, DPAs could provide PoC capability with single-step drop testing for analytical work in laboratories or in-field diagnostics for multiple major respiratory viruses while saving costs and improving healthcare. This work lays the foundation of this new technological platform that can provide a seamless transition from research to in-field application with a potential to alter the way modern diagnostics and precision medicine are practised.

Methodology

Fabrication of Templates

The TPS used are generated by first producing polycarbonate templates. These templates are created by first writing a pattern in PMMA using electron beam lithography (Raith) and then electroplating to generate a Ni shim. The shim is used as the master in the injection moulding to produce polycarbonate microscope slides with nano indented surfaces, that are the templates for the plasmonic metafilms. These templates are coated with a thin layer of gold (120 nm) through electron beam deposition (MEB-550s Plassys) to provide the metafilm that completes the TPS. Each TPS is then cleaned in a 25 Watt plasma oxygen asher for 30sec prior to any functionalisation. A customised fluidic well (GraceBio) with a glass cover slip is attached to the surface of the TPS for experimentation.

Optical Measurements

A custom-built microscope is used to image the TPS surfaces using a CMOS camera (FLIR) with a polariser, and a monochromatic light source (Spectral Photonics). LabVIEW software is used to control the light source wavelength and capture data from 18 locations in the image, corresponding to the nanoarrays on the TPS, and generate the dispersion spectrums. The software calculates the peak positions and a table is generated for all 18 locations to provide resonance peak wavelength values. Samples are placed on a stage with multi axis alignment features and alignment was performed to achieve even illumination and ORD with equal and opposite graphs from both left handed and right handed nanostructure arrays. For each experimental step, 3 measurements were taken (of all nanopatterned arrays) and the average was used to measure the resonance position for

each location. Graphs for each step were produced using the mean and standard deviation for all 18 locations.

Water and Salt Solution Experiments

A 2 M MgSO_4 solution was prepared in water. An initial reference measurement is taken using water pipetted into the fluidic well. An initial measurement was taken at 0 minutes, and every 30 minutes thereafter. After 3 hrs, the water is removed and the salt solution is added for measurements at 0 minutes, and every 30 minutes thereafter.

Streptavidin Experiments

Solution for the self-assembled monolayer (SAM) functionalisation were prepared using a 1:4 ratio of Biotin(PEG) Thiol: MT(PEG)₄ Thiol (Polypure 41156-1095; ThermoFisher 26132) with the constituents having a total 100 mM concentration in phosphate buffer saline (PBS, ThermoFisher). The sample was incubated in this solution for 24 h, followed by rinsing with PBS and measurements with PBS, for the starting reference values. Streptavidin (ThermoFisher 21122), at 1 μM , was prepared in PBS and added to the sample for 2 h. Measurements were taken before and after PBS rinsing. 1 μM Atto-655-Biotin (Sigma-Aldrich 06966) was also prepared in PBS and added to the sample for a further 2 hr period. Again, measurements were taken pre- and post-rinsing using PBS.

S1 Protein Experiments

The SAM was prepared using a 1:4 ratio of $\text{HS}-(\text{CH}_2)_{11}\text{-EG}_3\text{-NTA}$: $\text{HS}(\text{CH}_2)_{11}(\text{OCH}_2\text{CH}_2)_3\text{OH}$ (Prochimia TH007-002; Sigma-Aldrich 673110), with the constituents having a total concentration of 1 mM in 95% ethanol. Following 4-5 h incubation of the samples in this solution, they were rinsed with 95% ethanol and incubated for a further 5 minutes in 1 mM aqueous NaOH. The samples were then rinsed with water and incubated in 40 mM NiSO_4 for 1 hr. Finally, the samples were rinsed with HEPES buffered saline (HBS) and water and dried with nitrogen. The fluidic chamber was attached and an initial reference measurement was taken of the SAM following rinsing with PBS and Tween20 (surfactant rinsing solution). The 125 kDa recombinant human coronavirus SARS-CoV-2 Spike glycoprotein S1 (Abcam ab273068) was prepared at a concentration of 0.2 μM in PBS and applied to the sample for 1 hr. Measurements were taken with the anchored S1 on the surface pre- and post-rinsing. A solution of 0.2% (w/v) mucin from bovine submaxillary glands (Sigma-Aldrich M3895), 0.25 mg/ml haptoglobin (Merck Sigma-Aldrich #H3536) and 0.50 mg/ml transferrin (Merck Sigma-Aldrich T3309) artificial mucus was prepared in PBS and added to the sample for 15 minutes and biosensing measurements taken. 0.2 μM anti-SARS-CoV-2 spike glycoprotein S1 Ab (Abcam ab275759) in artificial mucus was applied to the sample for 1 hr. The protein-protein interaction was measured pre- and post-rinsing.

For the multiplexing setup, the SAM was prepared in a 1:4 ratio as before. A 1 μM solution of S1 protein (Abcam ab273068) in PBS was prepared, and 0.5 μL was spotted onto specific regions of the TPS. Recombinant His-tagged streptavidin, (Prospec Pro-621) was also prepared at 1 μM in PBS and spotted onto another two regions of the TPS. These solutions were left on the sample for 1 hr, followed by PBS and Tween20 rinsing. A fluidic chamber was then attached and measurements were performed. 1 μM anti-streptavidin antibody (Sigma-Aldrich S6390) was prepared in PBS and added to the sample for a 1 hr period, followed by addition of 1 μM anti-S1 antibody (Abcam ab275759) for a further 1 hr. Measurements were taken for both antibodies pre- and post-rinsing.

Isolation of SARS-CoV-2 Virus from Clinical Sample

SARS-CoV-2-CVR-GLA-8 virus (the clinical isolate Gla8) was isolated from nasal swabs from SARS-CoV-2-infected individuals that were obtained in viral transport medium (VTM) mixed 1:4 in Dulbecco's Modified Eagle Medium (DMEM) supplemented with 2% fetal calf serum (FCS), 1% Penicillin-Streptomycin and 250ng/ml Amphotericin B (ThermoFisher scientific, cat# 10566016, 10499044, 15140122 and 15290018, respectively). The mixture was clarified at 3000rpm for 10mins and then used to inoculate Vero E6 cells (African Green monkey kidney cell line, from Michelle Bouloy, Institute Pasteur, France) in a 6 well plate. Samples were harvested between 48 and 96 h post infection, depending on the extent of cytopathic effect (CPE). Viral presence was determined using a NEB Luna Universal Probe One-Step RT-qPCR Kit (New England Biolabs, E3006) and 2019-nCoV CDC N1 primers and probes (IDT, 10006713) and infectious titres by plaque assay. The viral sequence and the purity of the primary isolate were assessed using metagenomic next generation sequencing. Briefly, RNA was extracted from culture supernatant using a standard hybrid Trizol-RNeasy protocol (ThermoFisher scientific cat# 15596018). Library preparations were completed from cDNA using Kapa LTP Library Preparation Kit for Illumina Platforms (Kapa Biosystems, cat# KK8232). The sequencing of the libraries was carried out on Illumina's NextSeq 550 System (Illumina, cat# SY-415-1002). The resulting viral stock was designated CVR-GLA-8 (Genbank accession ON911332).

A virus working stock of CVR-GLA-8 was grown on A549-ACE2-TMPRSS2 and Vero E6 cell line as described previously.⁴³ The cells were maintained in DMEM-Glutamax supplemented with 10% fetal calf serum (FCS; Gibco) and non-essential amino acids (NEAA; Gibco) at 37°C in 5%(v/v) CO₂, humidified incubator. Infections were carried out with the SARS-CoV-2-CVR-GLA-8 in monolayers of the Vero E6 cells, in medium supplemented with 2% FCS, and incubated at 32°C for 7 days, after which medium containing infectious virus was harvested. To assess the infectious titre, A549-ACE2-TMPRSS2 or Vero E6 cells in 12-well plates were infected with 10-fold dilutions of virus samples. After 1 hour incubation at 37°C, 1 ml of overlay comprising MEM, 2% FCS, 0.6 % Avicel (Avicel microcrystalline cellulose, RC-591) was added per well and incubated at 37°C for 3 days. Cell monolayers were fixed with 8 % formaldehyde and plaques were visualized by staining with 0.1% Coomassie Brilliant Blue (BioRad cat# 1610406) in 45% methanol and 10% glacial acetic acid. CVR-GLA-8 stock titre on A549-ACE2-TMPRSS2 cells was 7.3×10^5 PFU/ml, and 5.3×10^4 PFU/ml on Vero E6 cells.

SARS-CoV-2 Inactivated Virus Experiments

Anti-SARS-CoV-2 spike glycoprotein S1 antibody (Abcam ab275759) was cleaved using a Pierce F(ab')₂ Micro Preparation kit (ThermoFisher 44688) following manufacturer instructions, with the estimated antibody fragmentation being between 50-70%. Concentration calculations assume 50% conversion. Following this preparation, the F(ab')₂ fragment solution was added for 1 hr, and a measurement was taken (concentrated). A 2mM MT(PEG)₄ spacer solution was prepared in PBS and was added for 1 hr. Measurements were then taken pre- and post-rinsing with PBS.

Virus was inactivated by addition of 0.2 ml of formaldehyde (Fisher Scientific cat# F/1501/PB17) to 1 ml of virus (final formaldehyde concentration 6% (v/v)). After 30 min incubation at room temperature inactivated virus solution was removed from the CL3. Inactivated virus was stored at -20°C until further use. The inactivated virus was diluted 1:1 with TRIS buffer to quench the formaldehyde prior to application. The final solution was added to the fluidic chamber for 1 hr, and measurements were taken prior to and after rinsing with PBS.

All live virus procedures were performed in a Biosafety level 3-laboratory at the MRC-University of Glasgow Centre for Virus Research (SAPO/223/2017/1a).

Acknowledgements

The authors would like to acknowledge the support by: EPSRC through grants EP/S001514/1, EP/S029168/1 and through the QuantIC funding scheme; MRC through a fellowship (MR/N008618/1 and MR/V035789/1), MRC CoV supplement grant (MC_PC_19026) and the Wellcome Trust Early Concepts in Development Scheme (219390/Z/19/Z). We like to acknowledge CRUSH (COVID-19 Drug Screening and Resistance Hub) at the University of Glasgow that generated and inactivated stock of SARS-CoV-2 for this study. We would also like to acknowledge support by industrial collaborators Avacta Lifesciences and Horiba Lifesciences (Paris).

References

- (1) Ginsburg, G. S.; Phillips, K. A. Precision Medicine: From Science To Value. *Health Aff* **2018**, *37* (5), 694–701. <https://doi.org/10.1377/hlthaff.2017.1624>.
- (2) Slikker, W. Biomarkers and Their Impact on Precision Medicine. *Exp Biol Med* **2018**, *243* (3), 211–212. <https://doi.org/10.1177/1535370217733426>.
- (3) Guglielmi, G. Fast Coronavirus Tests: What They Can and Can't Do. *Nature* **2020**, *585* (7826), 496–498. <https://doi.org/10.1038/d41586-020-02661-2>.
- (4) Mercer, T. R.; Salit, M. Testing at Scale during the COVID-19 Pandemic. *Nat Rev Genet* **2021**, *22* (7), 415–426. <https://doi.org/10.1038/s41576-021-00360-w>.
- (5) Larremore, D. B.; Wilder, B.; Lester, E.; Shehata, S.; Burke, J. M.; Hay, J. A.; Tambe, M.; Mina, M. J.; Parker, R. Test Sensitivity Is Secondary to Frequency and Turnaround Time for COVID-19 Screening. *Sci Adv* **2021**, *7* (1), 2020.06.22.20136309. <https://doi.org/10.1126/sciadv.abd5393>.
- (6) Taipale, J.; Kontoyiannis, I.; Linnarsson, S. Population-Scale Testing Can Suppress the Spread of Infectious Disease. *medRxiv* **2021**, 2020.04.27.20078329. <https://doi.org/10.1101/2020.04.27.20078329>.
- (7) Li, Z.; Leustean, L.; Inci, F.; Zheng, M.; Demirci, U.; Wang, S. Plasmonic-Based Platforms for Diagnosis of Infectious Diseases at the Point-of-Care. *Biotechnol Adv* **2019**, *37* (8), 107440. <https://doi.org/10.1016/j.biotechadv.2019.107440>.
- (8) Gupta, N.; Augustine, S.; Narayan, T.; O'Riordan, A.; Das, A.; Kumar, D.; Luong, J. H. T.; Malhotra, B. D. Point-of-Care PCR Assays for COVID-19 Detection. *Biosensors (Basel)* **2021**, *11* (5), 141. <https://doi.org/10.3390/bios11050141>.
- (9) Koczula, K. M.; Gallotta, A. Lateral Flow Assays. *Essays Biochem* **2016**, *60* (June), 111–120. <https://doi.org/10.1042/EBC20150012>.
- (10) He, P. J. W.; Katis, I. N.; Eason, R. W.; Sones, C. L. Rapid Multiplexed Detection on Lateral-Flow Devices Using a Laser Direct-Write Technique. *Biosensors (Basel)* **2018**, *8* (4). <https://doi.org/10.3390/BIOS8040097>.

- (11) Anker, J. N.; Hall, W. P.; Lyandres, O.; Shah, N. C.; Zhao, J.; van Duyne, R. P. Biosensing with Plasmonic Nanosensors. *Nanoscience and Technology: A Collection of Reviews from Nature Journals* **2009**, 308–319. https://doi.org/10.1142/9789814287005_0032.
- (12) Riedel, T.; Surman, F.; Hageneder, S.; Pop-Georgievski, O.; Noehammer, C.; Hofner, M.; Brynda, E.; Rodriguez-Emmenegger, C.; Dostálek, J. Hepatitis B Plasmonic Biosensor for the Analysis of Clinical Serum Samples. *Biosens Bioelectron* **2016**, *85*, 272–279. <https://doi.org/10.1016/j.bios.2016.05.014>.
- (13) Diao, W.; Tang, M.; Ding, S.; Li, X.; Cheng, W.; Mo, F.; Yan, X.; Ma, H.; Yan, Y. Highly Sensitive Surface Plasmon Resonance Biosensor for the Detection of HIV-Related DNA Based on Dynamic and Structural DNA Nanodevices. *Biosens Bioelectron* **2018**, *100*, 228–234. <https://doi.org/10.1016/j.bios.2017.08.042>.
- (14) Lopez, G. A.; Estevez, M. C.; Soler, M.; Lechuga, L. M. Recent Advances in Nanoplasmonic Biosensors: Applications and Lab-on-a-Chip Integration. *Nanophotonics* **2017**, *6* (1), 123–136. https://doi.org/10.1515/NANOPH-2016-0101/ASSET/GRAPHIC/J_NANOPH-2016-0101_FIG_003.JPG.
- (15) Peixoto de Almeida, M.; Pereira, E.; Baptista, P.; Gomes, I.; Figueiredo, S.; Soares, L.; Franco, R. Gold Nanoparticles as (Bio)Chemical Sensors. *Comprehensive Analytical Chemistry* **2014**, *66*, 529–567. <https://doi.org/10.1016/B978-0-444-63285-2.00013-4>.
- (16) Jarockyte, G.; Karabanovas, V.; Rotomskis, R.; Mobasher, A. Multiplexed Nanobiosensors: Current Trends in Early Diagnostics. *Sensors (Basel)* **2020**, *20* (23), 1–23. <https://doi.org/10.3390/S20236890>.
- (17) Mayer, K. M.; Hafner, J. H. Localized Surface Plasmon Resonance Sensors. *Chem Rev* **2011**, *111* (6), 3828–3857. https://doi.org/10.1021/CR100313V/ASSET/IMAGES/CR-2010-00313V_M029.GIF.
- (18) Gerion, D. Characterization and Performance of Commercial Localized Surface Plasmon Resonance Chips. *Plasmonics in Biology and Medicine IX* **2012**, 8234, 823412. <https://doi.org/10.1117/12.917241>.
- (19) Song, Y.; Huang, Y. Y.; Liu, X.; Zhang, X.; Ferrari, M.; Qin, L. Point-of-Care Technologies for Molecular Diagnostics Using a Drop of Blood. *Trends Biotechnol* **2014**, *32* (3), 132–139. <https://doi.org/10.1016/J.TIBTECH.2014.01.003>.
- (20) Karimullah, A. S.; Jack, C.; Tullius, R.; Rotello, V. M.; Cooke, G.; Gadegaard, N.; Barron, L. D.; Kadodwala, M. Disposable Plasmonics: Plastic Templated Plasmonic Metamaterials with Tunable Chirality. *Advanced Materials* **2015**, *27* (37), 5610–5616. <https://doi.org/10.1002/adma.201501816>.
- (21) Tullius, R.; Karimullah, A. S.; Rodier, M.; Fitzpatrick, B.; Gadegaard, N.; Barron, L. D.; Rotello, V. M.; Cooke, G.; Lapthorn, A.; Kadodwala, M. “Superchiral” Spectroscopy: Detection of Protein Higher Order Hierarchical Structure with Chiral Plasmonic Nanostructures. *J Am Chem Soc* **2015**, *137* (26), 8380–8383. <https://doi.org/10.1021/jacs.5b04806>.
- (22) Kelly, C.; Tullius, R.; Lapthorn, A. J.; Gadegaard, N.; Cooke, G.; Barron, L. D.; Karimullah, A. S.; Rotello, V. M.; Kadodwala, M. Chiral Plasmonic Fields Probe Structural Order of Biointerfaces. *J Am Chem Soc* **2018**, *140* (27), 8509–8517. <https://doi.org/10.1021/jacs.8b03634>.

- (23) Kakkar, T.; Keijzer, C.; Rodier, M.; Bukharova, T.; Taliansky, M.; Love, A. J.; Milner, J. J.; Karimullah, A. S.; Barron, L. D.; Gadegaard, N.; Lapthorn, A. J.; Kadodwala, M. Superchiral near Fields Detect Virus Structure. *Light Sci Appl* **2020**, *9* (1), 2047–7538. <https://doi.org/10.1038/s41377-020-00433-1>.
- (24) Tullius, R.; Platt, G. W.; Khosravi Khorashad, L.; Gadegaard, N.; Lapthorn, A. J.; Rotello, V. M.; Cooke, G.; Barron, L. D.; Govorov, A. O.; Karimullah, A. S.; Kadodwala, M. Superchiral Plasmonic Phase Sensitivity for Fingerprinting of Protein Interface Structure. *ACS Nano* **2017**, *11* (12). <https://doi.org/10.1021/acsnano.7b04698>.
- (25) Kelly, C.; Khosravi Khorashad, L.; Gadegaard, N.; Barron, L. D.; Govorov, A. O.; Karimullah, A. S.; Kadodwala, M. Controlling Metamaterial Transparency with Superchiral Fields. *ACS Photonics* **2017**, *5* (2), 535–543. <https://doi.org/10.1021/acsp Photonics.7b01071>.
- (26) Dadonaite, B.; Vijayakrishnan, S.; Fodor, E.; Bhella, D.; Hutchinson, E. C. Filamentous Influenza Viruses. *Journal of General Virology* **2016**, *97* (8), 1755–1764. <https://doi.org/10.1099/JGV.0.000535/CITE/REFWORKS>.
- (27) Jeong, H.-H.; Mark, A. G.; Alarcón-Correa, M.; Kim, I.; Oswald, P.; Lee, T.-C.; Fischer, P. Dispersion and Shape Engineered Plasmonic Nanosensors. *Nat Commun* **2016**, *7*, 11331. <https://doi.org/10.1038/ncomms11331>.
- (28) Chung, T.; Lee, S.-Y.; Song, E. Y.; Chun, H.; Lee, B. Plasmonic Nanostructures for Nano-Scale Bio-Sensing. *Sensors* **2011**, *11* (11), 10907–10929. <https://doi.org/10.3390/s111110907>.
- (29) Guo, L.; Jackman, J. A.; Yang, H.-H.; Chen, P.; Cho, N.-J.; Kim, D.-H. Strategies for Enhancing the Sensitivity of Plasmonic Nanosensors. *Nano Today* **2015**, *10* (2), 213–239. <https://doi.org/10.1016/j.nantod.2015.02.007>.
- (30) Luchansky, M. S.; Washburn, A. L.; Martin, T. A.; Iqbal, M.; Gunn, L. C.; Bailey, R. C. Characterization of the Evanescent Field Profile and Bound Mass Sensitivity of a Label-Free Silicon Photonic Microring Resonator Biosensing Platform. *Biosens Bioelectron* **2010**, *26* (4), 1283–1291. <https://doi.org/10.1016/J.BIOS.2010.07.010>.
- (31) Kötz, R.; Kolb, D. M.; Sass, J. K. Electron Density Effects in Surface Plasmon Excitation on Silver and Gold Electrodes. *Surf Sci* **1977**, *69* (1), 359–364. [https://doi.org/10.1016/0039-6028\(77\)90181-9](https://doi.org/10.1016/0039-6028(77)90181-9).
- (32) Wang, S.; Huang, X.; Shan, X.; Foley, K. J.; Tao, N. Electrochemical Surface Plasmon Resonance: Basic Formalism and Experimental Validation. *Anal Chem* **2010**, *82* (3), 935–941. https://doi.org/10.1021/AC902178F/ASSET/IMAGES/LARGE/AC-2009-02178F_0004.JPEG.
- (33) Chivers, C. E.; Koner, A. L.; Lowe, E. D.; Howarth, M. How the Biotin–Streptavidin Interaction Was Made Even Stronger: Investigation via Crystallography and a Chimaeric Tetramer. *Biochemical Journal* **2011**, *435* (1), 55–63. <https://doi.org/10.1042/BJ20101593>.
- (34) Ahlers, M.; Blankenburg, R.; Grainger, D. W.; Meller, P.; Ringsdorf, H.; Salesse, C. Specific Recognition and Formation of Two- Dimensional Streptavidin Domains in Monolayers: Applications to Molecular Devices. *Thin Solid Films* **1989**, *180* (1–2), 93–99. [https://doi.org/10.1016/0040-6090\(89\)90059-X](https://doi.org/10.1016/0040-6090(89)90059-X).

- (35) Weber, P. C.; Ohlendorf, D. H.; Wendoloski, J. J.; Salemme, F. R. Structural Origins of High-Affinity Biotin Binding to Streptavidin. *Science* (1979) **1989**, 243 (4887), 85–88. <https://doi.org/10.1126/science.2911722>.
- (36) Dong, J.; Zhang, Z.; Zheng, H.; Sun, M. Recent Progress on Plasmon-Enhanced Fluorescence. *Nanophotonics* **2015**, 4 (4), 472–490. <https://doi.org/10.1515/nanoph-2015-0028>.
- (37) Piran, U.; Riordan, W. J. Dissociation Rate Constant of the Biotin-Streptavidin Complex. *J Immunol Methods* **1990**, 133 (1), 141–143. [https://doi.org/10.1016/0022-1759\(90\)90328-S](https://doi.org/10.1016/0022-1759(90)90328-S).
- (38) González, M.; Bagatolli, L. A.; Echabe, I.; Arrondo, J. L. R.; Argaraña, C. E.; Cantor, C. R.; Fidelio, G. D. Interaction of Biotin with Streptavidin. *Journal of Biological Chemistry* **1997**, 272 (17), 11288–11294. <https://doi.org/10.1074/jbc.272.17.11288>.
- (39) le Trong, I.; Wang, Z.; Hyre, D. E.; Lybrand, T. P.; Stayton, P. S.; Stenkamp, R. E. Streptavidin and Its Biotin Complex at Atomic Resolution. *Acta Crystallogr D Biol Crystallogr* **2011**, 67 (9), 813–821. <https://doi.org/10.1107/S0907444911027806>.
- (40) Huang, Y.; Yang, C.; Xu, X.; Xu, W.; Liu, S. Structural and Functional Properties of SARS-CoV-2 Spike Protein: Potential Antivirus Drug Development for COVID-19. *Acta Pharmacol Sin* **2020**, 41 (9), 1141–1149. <https://doi.org/10.1038/s41401-020-0485-4>.
- (41) Mahmood, Z.; Alrefai, H.; Hetta, H. F.; A. Kader, H.; Munawar, N.; Abdul Rahman, S.; Elshaer, S.; Batiha, G. E.-S.; Muhammad, K. Investigating Virological, Immunological, and Pathological Avenues to Identify Potential Targets for Developing COVID-19 Treatment and Prevention Strategies. *Vaccines (Basel)* **2020**, 8 (3), 443. <https://doi.org/10.3390/vaccines8030443>.
- (42) Janeway, C. A.; Traver, P.; Walport, M. The Structure of a Typical Antibody Molecule. In *Immunobiology: The Immune System in Health and Disease*; Garland Science, 2001.
- (43) Rihn, S. J.; Merits, A.; Bakshi, S.; Turnbull, M. L.; Wickenhagen, A.; Alexander, A. J. T.; Baillie, C.; Brennan, B.; Brown, F.; Brunker, K.; Bryden, S. R.; Burness, K. A.; Carmichael, S.; Cole, S. J.; Cowton, V. M.; Davies, P.; Davis, C.; de Lorenzo, G.; Donald, C. L.; Dorward, M.; Dunlop, J. I.; Elliott, M.; Fares, M.; da Silva Filipe, A.; Freitas, J. R.; Furnon, W.; Gestuveo, R. J.; Geyer, A.; Giesel, D.; Goldfarb, D. M.; Goodman, N.; Gunson, R.; James Hastie, C.; Herder, V.; Hughes, J.; Johnson, C.; Johnson, N.; Kohl, A.; Kerr, K.; Leech, H.; Lello, L. S.; Li, K.; Lieber, G.; Liu, X.; Lingala, R.; Loney, C.; Mair, D.; McElwee, M. J.; McFarlane, S.; Nichols, J.; Nomikou, K.; Orr, A.; Orton, R. J.; Palmarini, M.; Parr, Y. A.; Pinto, R. M.; Raggett, S.; Reid, E.; Robertson, D. L.; Royle, J.; Cameron-Ruiz, N.; Shepherd, J. G.; Smollett, K.; Stewart, D. G.; Stewart, M.; Sugrue, E.; Szemiel, A. M.; Taggart, A.; Thomson, E. C.; Tong, L.; Torrie, L. S.; Toth, R.; Varjak, M.; Wang, S.; Wilkinson, S. G.; Wyatt, P. G.; Zusinaite, E.; Alessi, D. R.; Patel, A. H.; Zaid, A.; Wilson, S. J.; Mahalingam, S. A Plasmid DNA-Launched SARS-CoV-2 Reverse Genetics System and Coronavirus Toolkit for COVID-19 Research. *PLoS Biol* **2021**, 19 (2), e3001091. <https://doi.org/10.1371/JOURNAL.PBIO.3001091>.

TOC

